5-2018

Light Availability and Phytoplankton Growth Beneath Arctic Sea Ice: Integrating Observations and Modeling

Victoria J. Hill
Old Dominion University, vhill@odu.edu

Bonnie Light

Michael Steele

Richard C. Zimmerman
Old Dominion University, rzimmerm@odu.edu

Original Publication Citation

Hill, V. J., Light, B., Steele, M., & Zimmerman, R. C. (2018). Light availability and phytoplankton growth beneath Arctic sea ice: Integrating observations and modeling. *Journal of Geophysical Research: Oceans, 123*(5), 3651-3667. doi:http://dx.doi.org/10.1029/2017JC013617

Journal of Geophysical Research: Oceans

RESEARCH ARTICLE
10.1029/2017JC013617

Light Availability and Phytoplankton Growth Beneath Arctic Sea Ice: Integrating Observations and Modeling

Victoria J. Hill[1], Bonnie Light[2], Michael Steele[2], and Richard C. Zimmerman[1]

[1]Department of Ocean, Earth and Atmospheric Sciences, Old Dominion University, Norfolk, VA, USA, [2]Polar Science Center, Applied Physics Laboratory, University of Washington, Seattle, WA, USA

Key Points:
- An autonomous drifting buoy system was used to observe light and phytoplankton biomass under first-year sea ice and open water on the Beaufort-Chukchi shelf
- Drifting point observations captured the integrated response of phytoplankton to seasonally varying light fields
- An under-ice bloom was observed, and modeling suggested that in situ irradiance was sufficient to support net photosynthesis and growth

Supporting Information:
- Supporting Information S1

Correspondence to:
V. Hill,
vhill@odu.edu

Citation:
Hill, V. J., Light, B., Steele, M., & Zimmerman, R. C. (2018). Light availability and phytoplankton growth beneath Arctic sea ice: Integrating observations and modeling. *Journal of Geophysical Research: Oceans*, *123*, 3651–3667. https://doi.org/10.1029/2017JC013617

Received 4 NOV 2017
Accepted 4 APR 2018
Accepted article online 30 APR 2018
Published online 22 MAY 2018

Abstract Observations of the seasonal light field in the upper Arctic Ocean are critical to understanding the impacts of changing Arctic ice conditions on phytoplankton growth in the water column. Here we discuss data from a new sensor system, deployed in seasonal ice cover north-east of Utqiaġvik, Alaska in March 2014. The system was designed to provide observations of light and phytoplankton biomass in the water column during the formation of surface melt ponds and the transition from ice to open water. Hourly observations of downwelling irradiance beneath the ice (at 2.9, 6.9, and 17.9 m depths) and phytoplankton biomass (at 2.9 m depth) were transmitted via Iridium satellite from 9 March to 10 November 2014. Evidence of an under-ice phytoplankton bloom (Chl a $\sim$8 mg m^{-3}) was seen in June and July. Increases in light intensity observed by the buoy likely resulted from the loss of snow cover and development of surface melt ponds. A bio-optical model of phytoplankton production supported this probable trigger for the rapid onset of under-ice phytoplankton growth. Once under-ice light was no longer a limiting factor for photosynthesis, open water exposure almost marginally increased daily phytoplankton production compared to populations that remained under the adjacent ice. As strong effects of climate change continue to be documented in the Arctic, the insight derived from autonomous buoys will play an increasing role in understanding the dynamics of primary productivity where ice and cloud cover limit the utility of ocean color satellite observations.

1. Introduction

The high albedo of sea ice and snow limit the transmittance of ultraviolet and visible light to the water column beneath the ice-covered ocean. As a result, changes in sea ice thickness, snow depth, ice extent, and the timing of ice growth and retreat lead to significant alterations in the magnitude of solar radiation introduced to the water column of the Arctic Ocean. After several decades of well-documented decline in Arctic sea ice cover, summertime ice extent is now $\sim$40% below that observed in the late 1970s (Comiso, 2012; Frey et al., 2015; Grebmeier et al., 2015b; Kwok & Rothrock, 2009). Extensive replacement of the multiyear pack ice with first-year ice has reduced average sea ice thickness across the Arctic by 65% from a mean of 3.59 m in 1975 to just 1.25 m in 2012 (Lindsay & Schweiger, 2015; Richter-Menge & Farrell, 2013). Younger sea ice typically accumulates less snow, and this has been shown for the western Arctic (Webster et al., 2014), although there can be regional differences in snow depth with much more snow in the Atlantic sector of the Arctic (Merkouriadi et al., 2017). Sea ice with less snow will melt faster and undergo a rapid transition to bare ice relative to multiyear ice (Perovich & Polashenski, 2012). The presence of snow cover in the spring typically limits light transmission to $\leq$5% of incident irradiance, irrespective of ice thickness (Grenfell & Perovich, 2004; Perovich, 2007), and this influence persists until snow melt. Once the snow cover is removed, light transmission through first-year (FY) ice is consistently higher than through multiyear ice (Light et al., 2015; Nicolaus et al., 2012, 2013). The undeformed surface of seasonal ice also encourages the spreading of melt ponds, allowing for pond areal fractions greater than 0.7 to be achieved (Polashenski et al., 2012). Melt ponds allow as much as 30–70% of incident surface irradiance to be transmitted to the underlying water column (Ehn et al., 2011; Hudson et al., 2013; Light et al., 2015), increasing solar heating and leading to enhanced melting. Thinner, more transparent ice is also weaker and more vulnerable to fracturing by wind-induced stress (Itkin et al., 2017). The extensive fracturing of the ice pack in early spring produces leads that expose the underlying ocean to solar radiation in otherwise low-light areas (Assmy et al., 2017; Bernhard et al., 2007).

The Arctic-wide replacement of thick multiyear sea ice with thinner, more transparent seasonal ice could result in an earlier initiation and prolonged window for seasonal phytoplankton growth. High concentrations of phytoplankton recently observed in the water column beneath ice as far as 100 km from the ice edge may indicate that phytoplankton growth can now be initiated and sustained beneath a seasonal ice cover (Arrigo et al., 2012; Assmy et al., 2017; Churnside & Marchbanks, 2015). Horvat et al. (2017) conclude that ice thinning has increased the prevalence of conditions conducive for under-ice blooms, such that as much as 30% of the ice-covered Arctic in July could now support phytoplankton growth. Although the partition between open water, Marginal Ice Zone (MIZ), and under-ice blooms may have little to no effect on total seasonal production (Palmer et al., 2014), alterations in the timing and duration of Arctic Ocean net primary production (NPP) can have implications for pelagic and benthic food webs (Ji et al., 2013; Leu et al., 2011; Soreide et al., 2010).

The observation of previously unrealized phytoplankton production under the ice pack suggests that estimates of annual Arctic-wide NPP derived from satellite observations of open water areas may significantly underestimate true NPP (Arrigo et al., 2014; Hill et al., 2017). To determine the magnitude of phytoplankton growth that can be supported by the light environment under the ice pack, in situ measurements are required that encompass the evolution of the under-ice light field before and throughout snowmelt and melt pond formation. However, early spring oceanographic observations of the ice-covered Arctic region are difficult to make from ships or manned ice camp platforms, and impossible from satellites. Autonomous systems capable of seasonal or annual scale measurements can bridge the gap that satellites and ships cannot cover. Ice-tethered systems have been used to document seasonal changes in albedo and spectral transmittance (Nicolaus et al., 2010a, 2010b; Wang et al., 2014, 2016), as well as seasonal and internal variability in algal biomass, euphotic zone depth, and light variation due to surface ice heterogeneity (Laney et al., 2014, 2017). While these systems were in ice that survived through the summer, it is becoming challenging to find deployment locations safe from ice melt, making it more probable that ice-tethered instruments will melt out of the ice during the summer, necessitating new designs that can survive this process.

The goal of this study was to measure the changing under-ice light field before, during, and after ice melt, investigating the response of phytoplankton biomass to the light environment and determining the potential for phytoplankton growth beneath the ice. To accomplish this objective, we developed and deployed a new autonomous observing system that was easily transported onto the ice by light aircraft and capable of making measurements both within and beneath the ice from late winter, through spring, surviving melting out of the ice to continue observations into the summer and fall. These observations were tested against a bio-optical model to evaluate the potential for the observed light field to support phytoplankton growth.

2. Materials and Methods

2.1. Buoy Configuration

The Warming and Irradiance Measurements (WARM) buoy system was engineered by Pacific Gyre Inc. and consisted of a surface float supporting a suite of thermistors, irradiance sensors, and a fluorometer mounted on a 20 m long conductive cable (Figure 1). Upward looking radiometers were positioned along the sensor string at 0.5, 1, 5, 10, and 20 m depth relative to sea level (Figure 1). LiCor LI-192 plane irradiance sensors measuring photosynthetically available radiation (PAR) were placed 0.5, and 1 m from the sea surface. Both of these sensors froze into the ice. LiCor sensors where chosen for these depths as their small size minimized shading effects for these closely spaced sensors. Four channel (412, 443, 555 nm, and PAR) Satlantic OCR 500 multispectral irradiance sensors were placed at 5, 10, and 20 m from the sea surface. Wavelengths were chosen to allow for the reconstruction of the spectral distribution of irradiance and to provide an independent observation of changes in concentrations of colored dissolved organic material (CDOM) and phytoplankton. A Sea-Bird/Wet Labs ECO triplet fluorometer was colocated with the OCR 500 at 5 m depth and configured to measure Chl *a* (ex/em 470/695 nm) fluorescence, dissolved organic material (DOM; ex/em 370/460) fluorescence and backscattering at 532 nm. The manufacturer-provided calibration specific for this sensor was used to calculate chlorophyll concentration ([Chl *a*] mg m^{-3}) and DOM fluorescence as ppb Quine Sulphate equivalents. Measurements from the radiometers and ECO sensors were collected every 30 s over a 5 min period at the start of each hour, the average and standard deviation were communicated via Iridium satellite network. An upward looking digital RGB camera was mounted at 20 m to record images

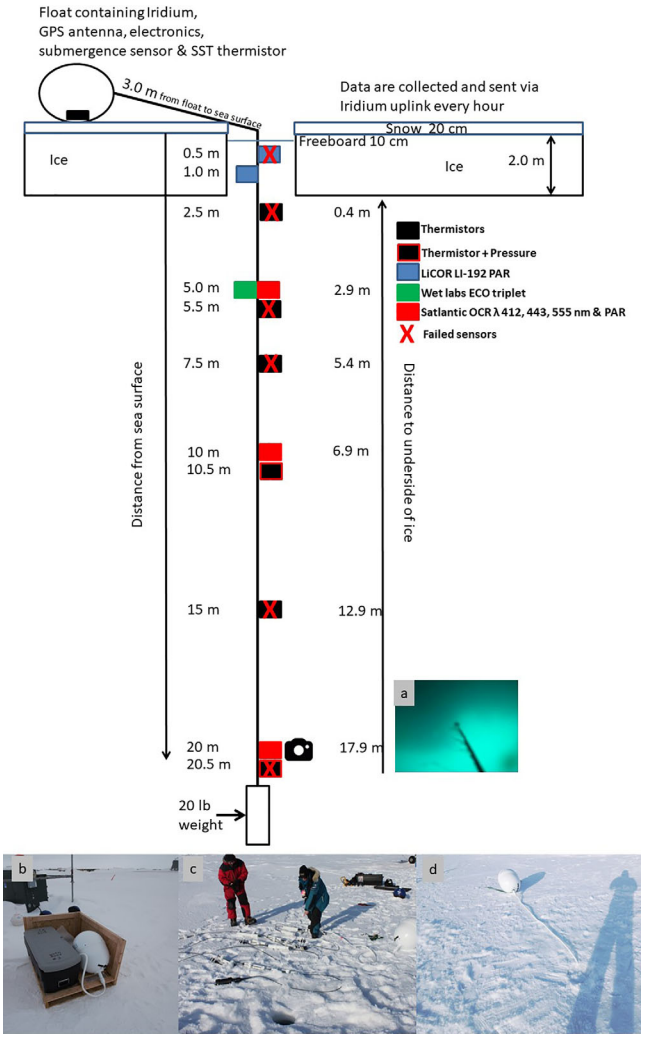

Figure 1. Diagram of the WARM buoy after deployment through the ice hole. Snow depth 20 cm, freeboard 10 cm, and ice thickness 2 m. When the system melted was floating in open water, sensor depths increased by 3 m as the surface float aligned vertically with the cable. (a) Example of daily image from upward looking camera and (b) Buoy in crate before deployment. (c) Buoy laid out on ice before deployment. (d) Buoy after deployment. Float is 136 cm in diameter and mass =∼ 23 Kg, total mass of the buoy and sensor string is ∼50 Kg. Pictures are from subsequent deployments, which were identical to #1.

of the underside of the ice, the water column, and the buoy cable each day near solar noon. Image resolution was 120 × 160 pixels, with a full-angle field of view of 53°, imaging an area of the under-ice surface was approximately 13 m by 17 m at initial depth of 20 m. Fouling accumulation (biological growth and particle deposition) on the sensors was unquantified, but the high fidelity of the camera images through time suggests that it was low. Strands of filamentous algae were visible on the cable above the camera in August, but never on the camera lens. Fouling would be expected to be minimal in the early spring when light and temperature were low. When present, biofouling would reduce the amount of light reaching the sensors, and dampen the response of the fluorometer, thereby degrading the relationship between K_dPAR and log Chl *a*. That relationship, however, remained constant throughout the observation period, suggesting minimal fouling of the sensor surfaces (supporting information Figure 1). Sedimentation of particles was considered to be of minimal concern on the ECO triplet due to the sensor's flat surface which permits particles to be washed away with mixing and current movement. Mechanical shutters were not employed on this system due to concerns regarding functionality at low temperature.

The sensors mounted along the cable communicated with the surface float using Seabird inductive modem technology. Power for the irradiance sensors was provided by a battery pack consisting of nine 1.5 V alkaline cells (size C) connected in series, providing 8 A h of electrical capacity at 13.5 V. The ECO Triplet was powered by two of these packs connected in parallel, providing ∼16A h at 13.5V (initial). The surface float, housed the controller, the transmitter and the surface sensors that were powered by two 32 cell packs in parallel to provide ∼112 A h at 12V (initial).

Data were transferred at hourly intervals to servers at Pacific Gyre Inc. using an Iridium 9602 modem and the Iridium satellite network. Failure of all thermistors (except the one at nominal 10 m depth position) and the 0.5 m radiometer occurred within 48 h of deployment and so are not reported here. Instrument failure was addressed and resolved in all subsequent deployments. All data from the buoy are available from the NSF Arctic Data Center (www.arcticdata.io; Hill et al., 2016). Data from this and other WARM buoys are also available in near real-time at the UpTempO and WARM buoy site at the University of Washington: http://psc.apl.washington.edu/UpTempO/Data.php.

2.2. Buoy Deployment

The buoy was ferried by helicopter to a ∼0.5 km^2 floe of generally flat ice ∼120 km ENE of Point Barrow, Alaska (71.573013, −153.071487) on 9 March 2014 (Figure 2). The ice was 2 m thick, and snow depth was 0.20 m, with a freeboard of 0.1 m. The sensor string was lowered through a 25 cm diameter hole drilled through the ice. The float was placed on the surface of the ice, offset ∼3 m from the hole to avoid shading the sensors (Figure 1) and held in place by straps and ice screws to prevent horizontal movement and vertical slippage until the hole refroze. Ice chips from the drilling process and snow were pushed back into the ice hole after deployment to accelerate refreezing. The gradual disappearance of the bright spot seen in the daily photographs between 9 and 13 March (Figures 3a and 3b) is postulated to be due to refreezing of the ice hole facilitated by air temperatures of ∼–25°C (Eicken, 2016) and likely drifting snow which reduced the light transmission.

Initial depths of the three in-water radiometers were 5, 10, and 20 m relative to the sea surface. As the ice melted in the summer, the ballast weight at the base of the sensor string pulled the surface float into

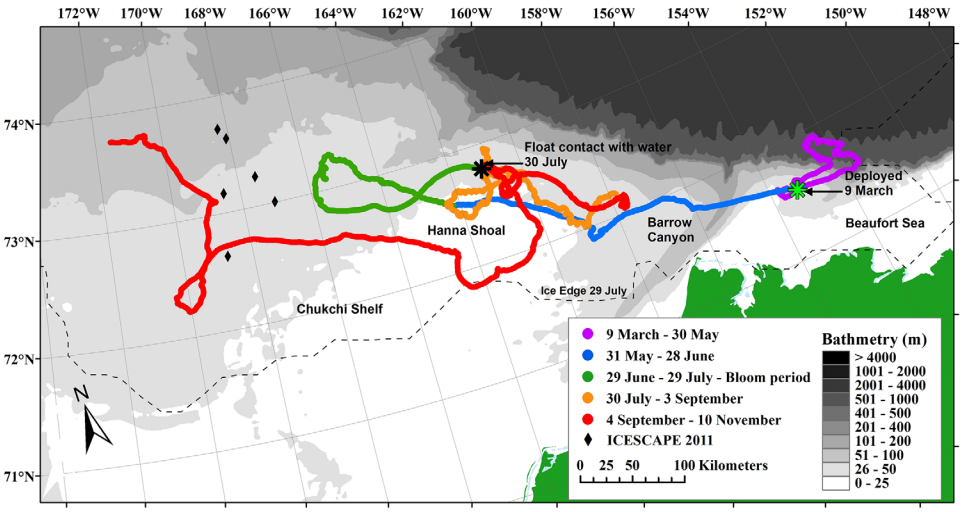

Figure 2. Map of the WARM buoy track during 2014 overlaid on the IBACO bathymetry (https://www.ngdc.noaa.gov/mgg/bathymetry/arctic). The green star indicates deployment location. The black star indicates the point that the float contacted water, which occurred on 30 July. The under-ice bloom was observed between 29 June and 29 July (green track). Locations of the ICESCAPE under-ice bloom observed in 2011 are indicated by black diamonds, as detailed in Arrigo et al., (2012). Location of 15% ice cover contour estimated from SSMIS data for 29 July represented as dashed line.

vertical alignment with the tether and increasing the depth of all sensors by 3 m (the initial offset of the float from the ice hole). A wet/dry sensor on the underside of the surface float indicated when the buoy was floating on the sea surface. Light levels dropped below detection limits on 10 November 2014, and the buoy stopped transmitting on 4 January 2015.

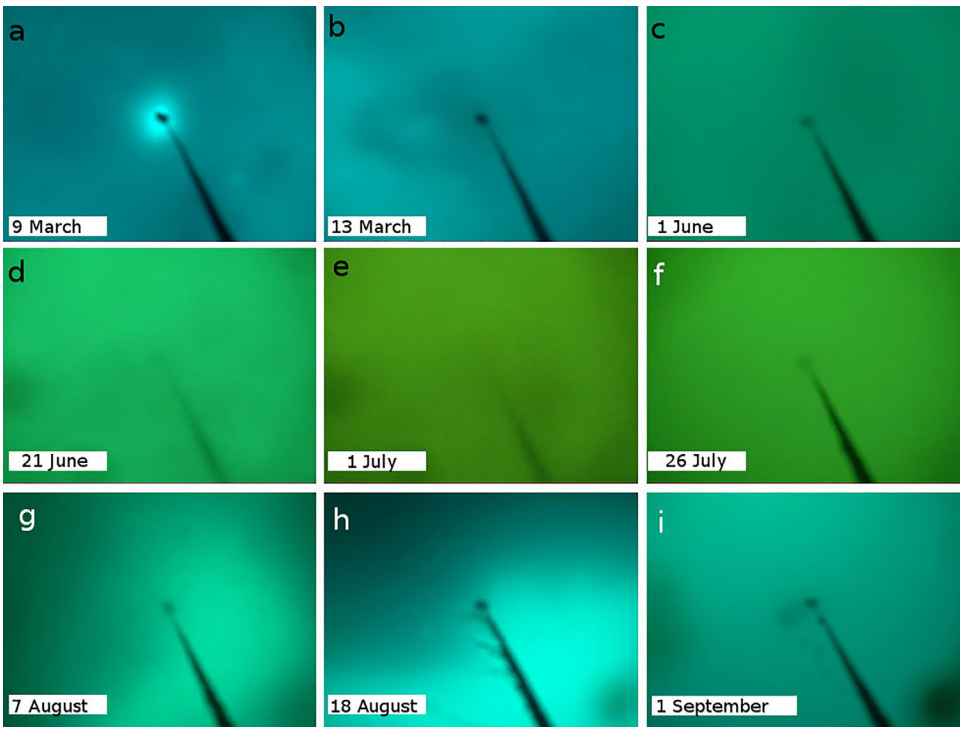

Figure 3. Time series of images looking up at ice bottom from 20 m depth. The black line in each image is the sensor string. Brighter areas in the field of view likely correspond to areas with reduced snow cover in the spring and surface melt ponds later in summer. The camera field of view was 53°, yielding a 13 m × 17 m image of the under-ice surface.

2.3. Ice Concentration and Distance to Ice Edge

Ice concentration proximal to the buoy was determined using the AMSR2 passive microwave sensor, available at daily, 3.125 km resolution from the University of Hamburg (Beitsch et al., 2014). The uncertainty of this algorithm was estimated for the older but similar AMSR-E sensor as ~25% near the ice edge, linearly improving toward ~6% in 100% pack ice (Spreen et al., 2008). We also used passive microwave data available from the SSMIS sensor at daily, 25 km resolution (Peng et al., 2013) with uncertainty of 5% in winter and 15% in summer The shortest distance from the buoy to the 15% ice concentration contour (i.e., the ice edge) was determined daily using the SSMIS data.

2.4. Data Analysis

Observed irradiance [$E_d(\lambda)$] values measured at each sensor were used to calculate the diffuse attenuation coefficient [$K_d(\lambda)$] according to Beer's Law:

$$K_d(\lambda) = \frac{\ln[E_d(\lambda, z_1)] - \ln[E_d(\lambda, z_2)]}{\Delta z} \quad (1)$$

where, $E_d(\lambda, z_1)$ and $E_d(\lambda, z_2)$ represent irradiances at the upper and lower sensors, respectively, and Δz is the difference in geometric depth between the sensors. Tilt information was not available for the sensors, the maximum daily depth change observed at the 10 m pressure sensor was 0.1 m during ice-tethered periods and 0.3 m in open water, indicating the wire was likely being dragged with minimal angle due to relative motion along the length of the cable. However, differentiation between wire angle and depth changes due to slippage, vertical ice movement, or atmospheric pressure was not possible. K_d for photosynthetically available radiation [K_d(PAR)] was calculated between 1 and 5, 5 and 10 m and 10 and 20 m depths. K_d at 412, 443, and 555 nm was only available between the OCR sensors at 5, 10, and 20 m. Only $E_d(\lambda)$ measured at solar noon was used to calculate $K_d(\lambda)$ for the time series to avoid complications from high solar zenith angles, which cause $K_d(\lambda)$ (an apparent optical property) to increase (Kirk, 1994). Occasionally, recorded values of $E_d(\lambda)$ were higher at 5 m than at 1 m (Figure 4b) indicating the presence of nearby melt ponds or cracks through which light illuminated the deeper sensor (Frey et al., 2011). This resulted in negative K_d values that were not representative of light attenuation by the water column. All [Chl *a*] values are reported at the highest solar zenith angle of the day to avoid the diurnal photoadaptation observed in the fluorescence signal. [Chl *a*] estimates between 10 and 20 m were derived from the strong relationship between K_d(PAR) between 5 and 10 m and [Chl *a*] observed during the deployment (supporting information Figure 1, log[Chl a] = 3.445 × K_d(PAR) − 0.69, r^2 = 0.91). This relationship was also used to cover gaps in ECO triplet communication from 6 June to 2 July.

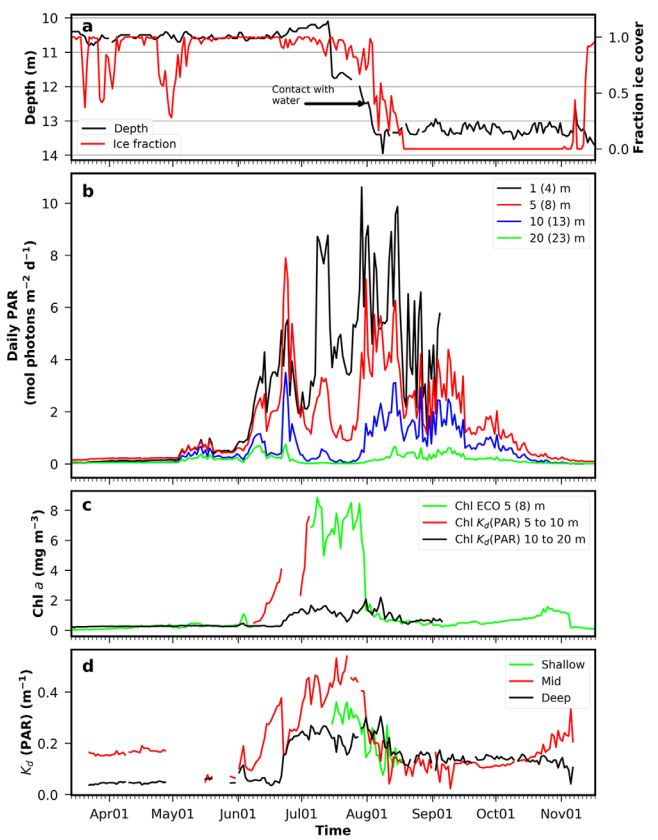

Figure 4. (a) Ice cover fraction calculated from the AMSR2 and SSMIS sensors. (b) Depth of the 10 m (initial depth) pressure sensor (black) and distance from the buoy to the ice edge calculated from the AMSR2 sensor (red). (c) Total daily PAR recorded by each sensor, approximate depths after melt out indicated in parentheses. (d) Chl *a* concentration observed at the lowest solar elevation of the day (to avoid photoadaptation bias in the fluorescence signal), and retrieved from the ECO triplet (green), from K_d(PAR) 5 to 10 m (red) and K_d(PAR) from 10 to 20 m (black). (e) Diffuse attenuation coefficient, K_d(PAR) calculated at the highest solar elevation of each day between each successive pair of PAR sensors. "Shallow" is calculated between 1 and 5 m and is only shown for the period after the 1 m sensor melted out of the ice, "Mid" was calculated between 5 and 10 m and "Deep" between 10 and 20 m. Colored plots represent the time periods from the buoy drift highlighted in Figure 2.

2.5. Modeling Under-Ice Potential Primary Production

Under-ice primary production was predicted from the water column light field using a spectrally resolved, vertical 2-D (depth × time) model of biomass-specific gross photosynthesis. All symbols and definitions used in the model are defined in Table 1.

2.5.1. Modeling the Underwater Light Field

Scalar irradiance [$E_o(\lambda, t, z)$] was calculated at 0.5 m vertical resolution and 1 h intervals for use in the primary production model using a two flow approximation. This was necessary as our observations did not provide measurements of inherent optical properties required to specify a full 3-D radiative transfer model such as *HydroLight* ©.

Journal of Geophysical Research: Oceans

10.1029/2017JC013617

Table 1
Summary of Symbols, Definitions, and Their Dimensional Units

Symbol	Definition	Value	Dimensions	Source	Representative conditions
Optical parameters					
$a_t(\lambda)$	Total absorption coefficient		m^{-1}	Equation (3)	
$a_w(\lambda)$	Pure water absorption coefficient		m^{-1}	Pope and Fry, (1997)	
$a_g(\lambda)$	CDOM absorption coefficient		m^{-1}	Equation (5)	
$a_\varphi(\lambda)$	Phytoplankton absorption coefficient		m^{-1}	Equation (6)	
$a^*_\phi(\lambda)$	Chlorophyll specific phytoplankton absorption		$m^2\ mg^{-1}$	Supporting information Figure S2	
$a_{p\text{-}\varphi}(\lambda)$	Non-algal absorption coefficient		m^{-1}	Equation (7)	
$b_b(\lambda)$	Total backscatter coefficient		m^{-1}	Equation (4)	
$b_{bw}(\lambda)$	Water backscattering coefficient		m^{-1}	Pope and Fry, (1997)	
$b_{bp}(\lambda)$	Particulate backscattering coefficient		m^{-1}	Equation (9)	
$E_d(\lambda, z_{0+})$	Downwelling irradiance spectra at the ice surface		$\mu mol\ m^{-2}\ s^{-1}$	Modeled using hydrolight	
$E_d(\lambda, z)$	Depth-resolved downwelling irradiance		$\mu mol\ m^{-2}\ s^{-1}$	Equation (12)	
$E_u(\lambda, z)$	Depth-resolved upwelling irradiance		$\mu mol\ m^{-2}\ s^{-1}$	Equation (14)	
$E_o(\lambda, t, z)$	Depth and time-resolved scalar irradiance		$\mu mol\ m^{-2}\ s^{-1}$	Equation (15)	
$E_d0\ (\lambda)$	downwelling irradiance spectra at the ice water interface		$\mu mol\ m^{-2}\ s^{-1}$	Calculated from buoy observations, time-varying.	
$E_{d\_back}(\lambda)$	Backwards scattered light		$\mu mol\ m^{-2}\ s^{-1}$	Equation (13)	
$K_d(\lambda)$	Downwelling diffuse attenuation coefficient		m^{-1}	Equation (2)	
$K_u(\lambda)$	Upwelling diffuse attenuation coefficient		m^{-1}	Equation (2)	
S_{NAP}	Spectral slope for absorption by non-algal particulates	0.005	Dimensionless	Wang et al., (2005)	Chukchi Sea
S_g	Spectral slope of CDOM absorption	0.02	Dimensionless	Hill and Zimmerman, (2016)	Arctic, spring
$\overline{\mu}_d$	Mean cosine of downwelling light		Dimensionless	Ehn and Mundy (2013); Katlein et al. (2014)	Under ice Arctic
$\overline{\mu}_u$	Mean cosine of upwelling light		Dimensionless		
Phytoplankton biomass, grazing sinking, and mixing parameters					
[Chl *a*]	Chlorophyll a concentration	0.01	$mg\ m^{-3}$	Set to initial value in model	
P^B_E	Biomass-specific rate of light-saturated photosynthesis	0.11	$mmol\ C\ mg\ Chl^{-1}\ h^{-1}$	Platt et al. (1982)	Diatoms, 50% light level, Baffin Bay, summer—ice-free
ϕ_P	Quantum yield of photosynthesis (O_2) for absorbed photons	0.125	mol O_2 mol photons absorbed^{-1}	Emerson and Lewis (1943) and Laws (1991)	
PQ	Photosynthetic quotient	1.2	mol O_2 evolved mol C fixed^{-1}	Laws (1991)	Polar phytoplankton
Φ_m	Quantum yield of photosynthesis (Carbon) for absorbed photons	0.104	mol C fixed mol photons absorbed^{-1}	$= \phi_P$ /PQ	
$A\phi^*(\lambda)$	Spectral absorptance		Dimensionless	Equation (6)	
P^B_g	Gross biomass-specific photosynthesis		$mg\ C\ mg\ Chl^{-1}\ h^{-1}$	Equation (16)	
P^B_{net}	Net biomass-specific photosynthesis		$mg\ C\ mg\ Chl^{-1}\ h^{-1}$	Equation (17)	
R^B	Biomass-specific respiration	5% of P^B_E	$mg\ C\ mg\ Chl^{-1}\ h^{-1}$	Forest et al. (2011)	Arctic values, lower end of range to represent cold temperatures
P^V_{net}	Volume-specific net photosynthesis		$mg\ C\ m^{-2}\ h^{-1}$	Equation (18)	
P^z_{gross}	Daily depth-integrated gross photosynthesis		$mg\ C\ m^{-2}\ d^{-1}$	Calculated in the model	
B	Phytoplankton biomass	0.05	$mmol\ C\ m^{-3}$	Initial setting for model	
G	Grazing	44% and 97% of net phytoplankton growth	$mg\ C\ m^{-3}$	Campbell et al. (2009); Verity et al. (2002); and Yang et al. (2015)	Chukchi Sea, Canada Basin (summer). Beaufort & Chukchi Seas (spring and summer). Barents Sea, summer
W_p	Sinking coefficient	0.1	$m\ d^{-1}$	Moran et al. (2005)	Chukchi Sea
κ_z	Water column eddy diffusivity coefficient	0.11×10^{-4}	$m^2\ s^{-1}$	Palmer et al. (2014)	Antarctica under ice

However, the spectral distribution of downwelling irradiance incident on the upper surface of the ice [$E_d(\lambda, z_{0+})$] was calculated using *HydroLight* for the relevant location and local time, assuming a cloud-free sky. The in-water spectral distribution of downwelling irradiance at the ice-water interface [$E_d(\lambda, z_0)$] was calculated by propagating $E_d(\lambda, z_{0+})$ through the ice using transmittance coefficients from Light et al. (2015). K_d values at 412, 443, and 555 nm calculated between 5 and 10 m were used to extrapolate observed E_d at 412, 443, and 555 nm at 5 m up to the underside of the ice, a distance of approximately 3 m. The previously calculated $E_d(\lambda, z_0)$ was then normalized to $E_d(555)$ at the underside of the ice to calculate the correct spectral shape and intensity of under ice irradiance at 0 m [$E_d(\lambda, z_0)$]. At each time step within the model, downwelling [$E_d(\lambda, z)$] and upwelling planar irradiance [$E_u(\lambda,z)$] through the water column were initialized at 0 m with $E_d(\lambda, z_0)$ and propagated with depth using downwelling [$K_d(\lambda)$] and upwelling diffuse attenuation coefficients [$K_u(\lambda)$]. $K_d(\lambda)$ was calculated from the absorption and scattering properties of water column components based on the following relationships developed by Lee et al. (2005 and 2007) and subsequently validated by Zimmerman et al. (2015) for optically complex coastal waters

$$K_d(\lambda)=(1+0.005\theta_0) * a_t(\lambda)+4.18 * \{1-0.52\exp[-10.8 * a_t(\lambda)]\} * b_b(\lambda) \quad (2)$$

where Θ_0 corresponds to the effective angle of solar radiation at the ice-water interface, assuming the average cosine of the downwelling light field ($\overline{\mu}_d$) just beneath the ice was 0.7 (Ehn & Mundy, 2013). The total absorption spectrum [$a_t(\lambda)$] was partitioned into absorption by seawater [$a_w(\lambda)$], colored dissolved organic material [$a_g(\lambda)$], phytoplankton [$a_\phi(\lambda)$], and nonalgal matter [$a_{p-\phi}(\lambda)$]:

$$a_t(\lambda)= a_w(\lambda)+a_g(\lambda)+a_\phi(\lambda)+a_{p-\phi}(\lambda) \quad (3)$$

The total backscatter coefficient [$b_b(\lambda)$] was separated into backscatter by seawater [$b_{bw}(\lambda)$] and particulates [$b_{bp}(\lambda)$]:

$$b_b(\lambda)=b_{bw}(\lambda)+b_{bp}(\lambda) \quad (4)$$

Absorption $a_w(\lambda)$ and scattering $b_{bw}(\lambda)$ by pure water were assumed to be constant with depth (Pope & Fry, 1997). The spectral absorption coefficient of a_g was expressed as a negative exponential function scaled by the absorption at 443 nm, which was set to a constant 0.065 m^{-1} (Hill, 2008):

$$a_g(\lambda)=a_g(443) * \exp[-S_g(\lambda-443)] \quad (5)$$

where the exponential term S_g (0.02) provided the spectral slope for absorption by a_g (Hill & Zimmerman, 2016). The spectral absorption coefficient for phytoplankton [$a_\phi(\lambda)$] was calculated from the average chlorophyll specific absorption spectrum, [$a^*_\phi(\lambda)$] (supporting information Figure 2) collected during the Shelf Basin Interactions Project in the Chukchi Sea during the spring and summer of 2002 and 2004 (Hill, 2004) and chlorophyll concentration as:

$$a_\phi(\lambda)=a^*_\phi(\lambda) * [\text{Chl } a] \quad (6)$$

The absorption coefficient of nonalgal particles at 443 nm [$a_{p-\phi}(443)$] was calculated as a function of [Chl *a*] (Bricaud et al., 1995; Roesler et al., 1989) and then used to calculate $a_{p-\phi}(\lambda)$ (equation (8)).

$$a_{p-\phi}(443)=0.0306\ [\text{Chl } a]^{0.296} \quad (7)$$

The spectral absorption coefficient for nonalgal particles [$a_{p-\phi}(\lambda)$] was then calculated as:

$$a_{p-\phi}(\lambda)=a_{p-\phi}(443) * \exp[-S_{NAP}(\lambda-443)] \quad (8)$$

where the exponential term S_{NAP} (0.005) provided the spectral slope for this absorption (Wang et al., 2005). The particulate backscattering at 555 nm (equation (9)) and the index of backscattering dependency (γ; equation (10)) were calculated using Chukchi Sea specific relationships (Wang et al., 2005) based on [Chl *a*].

$$b_{bp}(555)=0.004 * [Chl\ a]^{0.357} \quad (9)$$

$$\gamma=-2.348 * log_{10}(b_b(555))-4.353 \quad (10)$$

The spectrally resolved backscattering coefficient was then calculated following Reynolds et al., (2001).

$$b_b(\lambda) = b_{bw}(555) + b_{bp} * (555-\lambda)^{\gamma} \quad (11)$$

The downwelling plane irradiance leaving each vertical layer [$E_d(\lambda, z)$] was calculated as a function of the irradiance entering the layer [$E_d(\lambda, z+\Delta z)$], $K_d(\lambda)$ and thickness of the layer (Δz). $E_d(\lambda, z_0)$ calculated above was used to initialize the light at 0 m for time each step:

$$E_d(\lambda, z) = E_d(\lambda, z+\Delta z)^{-K_d(\lambda)*\Delta z} \quad (12)$$

Light backscattered in the upward direction [$E_{d\text{-}back}(\lambda, z)$] within each layer of the model was expressed as:

$$E_{d\_back}(\lambda, z) = E_d(\lambda, z) * b_b(\lambda, z) \quad (13)$$

Upwelling irradiance in each layer was calculated by first setting $E_u(\lambda)$ in the bottom-most layer to $E_{d\_back}(\lambda)$ within that layer. $E_u(\lambda)$ in each successive layer was then calculated as the sum of $E_u(\lambda)$ entering from the layer below, attenuated using K_u (which was taken to be equal to K_d) and the backscattered light within each layer. Thus $E_u(\lambda)$ at 10 m would be calculated as:

$$E_u(10\ m) = E_u(10.5\ m)^{-K_u(\lambda)*\Delta z} + E_{d\_back}(10\ m) \quad (14)$$

Finally, scalar spectral irradiance [$E_o(\lambda, z)$] was calculated as the sum of E_d and E_u in each layer as a function of the average cosines of the downwelling ($\overline{\mu}_d$) and upwelling light field ($\overline{\mu}_u$):

$$E_0(\lambda, z) = \frac{E_d}{\overline{\mu}_d}(\lambda, z) + \frac{E_u}{\overline{\mu}_u}(\lambda, z) \quad (15)$$

$\overline{\mu}_d$ was calculated using a relationship between scattering to absorption ratio and sun angle, based on a relationship defined by Kirk (1994) where $\overline{\mu}_d$ at the underside of the ice was initialized at 0.7 (Ehn & Mundy, 2013; Katlein et al., 2014) decreasing to minimum of 0.6 as b/a increased. $\overline{\mu}_u$ was set to a constant value of 0.45 to represent the typical angular distribution of upwelling irradiance in optically deep water that is slightly brighter in the horizontal than the vertical.

2.5.2. Modeling Primary Production

$E_0(\lambda, t, z)$ was used to calculate phytoplankton photosynthesis using a spectrally resolved, depth-dependent model of biomass-specific gross photosynthesis $\left(P_g^B\right)$:

$$P_g^B = P_E^B\left[1 - \exp\left(\frac{-\phi_m * A_\phi^*(\lambda) * [Chl\ a] * (\lambda, t, z)}{P_E^B}\right)\right] \quad (16)$$

where P_E^B represents the biomass-specific rate of light-saturated photosynthesis and was set to an Arctic-specific value of 0.11 mmol C mg Chl^{-1} h^{-1} (Table 1; Platt et al., 1982 and references therein). The quantum yield of photosynthesis for absorbed photons (ϕ_m) was set equal to 0.104 mol C mol^{-1} photons absorbed based on the theoretical maximum quantum yield of 0.12 mol O_2 mol^{-1} photons absorbed, and photosynthetic quotient of 1.2 mol O_2 evolved mol^{-1} C fixed (Table 1; Emerson & Lewis, 1943; Laws, 1991). Spectral absorptance [$A\phi^*(\lambda)$] was derived from $a_\phi(\lambda)$ (equation (6)) as 1–exp[–$a_\phi(\lambda)$]. Spectral scalar irradiance [$E_o(\lambda,t,z)$] was determined as above (equaitons (2)–(15)). Net photosynthesis was calculated as the balance between light-dependent photosynthesis (equation (16)) and respiration,

$$P_{net}^B = P_g^B - R^B \quad (17)$$

where the biomass-specific respiration (R^B) was set to 5% of P_E^B (Forest et al., 2011), which is representative of reduced respiration at low temperatures (Vaquer-Sunyer et al., 2010). The terms in equation (17) were then multiplied by phytoplankton biomass (B; mol C m^{-3}) to obtain volume-specific rates. Biomass was calculated using a molar ratio of 60:1 for Carbon: Chl a:

$$P_{net}^V = B\left[P_g^B - R^B\right] \quad (18)$$

Redfield Ratios were used to define dissolved inorganic nitrogen (N) and phosphorus (P) required to convert net photosynthesis $\left(P_{net}^V\right)$ into new biomass. If concentrations of either N or P were insufficient to satisfy the demand based on net photosynthesis, then phytoplankton growth was restricted by the most limiting nutrient. Any fixed carbon that was not used for growth was kept as an internal reserve to support respiration whenever $P_{net}^B < R$. If carbon reserves were insufficient, the remainder of the respiratory demand was met by

mobilizing the structural carbon pool of the phytoplankton. In addition to reducing phytoplankton biomass, the respiration of structural carbon also remineralized nitrogen and phosphorus in proportion to the Redfield ratio, which could be reassimilated at subsequent time steps.

Zooplankton grazing was dependent on net phytoplankton growth (Yang et al., 2015). Two grazing simulations were considered, low grazing at 44% of net primary production (Campbell et al., 2009) and high grazing at 97% of net primary production (Verity et al., 2002; Yang et al., 2015). Grazing was set to 0 when [Chl *a*] < 4 mg m^{-3}, based on the assumption that the zooplankton population would be minimal before the onset of the spring bloom. Grazing was assumed to follow an exponential function between zero grazing, and the maximal grazing rate reached when Chl was $<= 5$ mg m^{-3}. Testing of the [*Chl a*] threshold used to initate grazing showed a 1 day delay in the timing of the bloom peak when grazing was started at 3 mg m^{-3}, and a 2 day delay when grazing was intiaited at 0.01 mg m^{-3} at 1% increasing to 44% at 4 mg m^{-3}. Due to the small diffrences in model output, these results are not shown. Scenarios with remineralization rate of 80% and 90% of grazed biomass were considered in which NH_4^+ and PO_4^{-3} were remineralized back into the water column pools in proportion to the Redfield ratio, the remainder (20% or 10%) was assimilated into the zooplankton pool.

The model was run with 1 h time steps from 1 May to 31 August 2014. Initial conditions were set to a vertically homogeneous [Chl *a*] distribution of 0.01 mg m^{-3} (0.05 mg C m^{-3}), representative of late winter concentrations. Initial concentrations of NH_4^+ (3 mmol m^{-3}), NO_3^- (10 mmol m^{-3}), and PO_4^{-3} (2 mmol m^{-3}) were taken from Codispoti et al., (2013). At the end of each timestep, biomass was mixed vertically using an eddy diffusion coefficient of $\kappa_z = 0.11 \times 10^{-4}$ m^2 s^{-1}. κ_z represents the cumulative effect of all turbulent mixing in the surface ocean mixed layer (here inclusive of the 20 m maximum depth of model) and the value used is the midrange for under-ice measurements from the Amundsen Gulf and used in previous models for the Arctic (Palmer et al., 2014). A sinking coefficient for phytoplankton (W_p) of 0.1 m d^{-1} was used based on field observations (Moran et al., 2005).

2.5.3. Modeling the Impact of Open Water on Primary Production

The impact of open water on daily incident PAR and water column integrated gross photosynthesis for a 24 h period in July was determined by running the primary production model for 600 permutations of open water duration (0–24 h) and start time (midnight to midnight). Downwelling spectral irradiance for open water was modeled using *HydroLight* © for the relevant location and local time, assuming a cloud-free sky. As clouds exert a complex, temporally unpredictable influence on radiation intensity (Matuszko, 2012), these simulations were run in a cloud-free setting. As such, they represent the upper limits of light availability and carbon uptake. Irradiance at the water surface for each hour of the 24 h period was then set to either the open water value or the under-ice spectral irradiance calculated in section 2.5.1 dependent on the permutation of open water versus under ice.

3. Results

3.1. Buoy Track

After deployment on 9 March in the western Beaufort Sea (Figure 2), ice fraction around the buoy (SSMIS pixel size 25 km) remained between 0.9 and 1.0 (Figure 4a). Ice fraction using the higher resolution (AMSR2 3.1255 km) dropped below 0.5 at the end of March and again at the end of April, showing the effects of a large polynya that formed around Point Barrow (Figure 4a). Between 6 and 30 May, the buoy drifted NE toward the shelf break, before turning south-west and crossing the mouth of Barrow Canyon on 31 May. The buoy then continued to drift westward, crossing Hanna Shoal during June and remained approximately 150 km north of the ice edge (Figure4b). In July, the buoy track made a loop just west of Hanna Shoal. Ice fraction started to decline in mid-July, reaching zero in mid-August (Figure4a) as the ice edge advanced northward of the buoy leaving it in open water (Figures 4a and 4b). The tether slipped abruptly through the ice on 13 July when the depth recorded at the pressure sensor increased from 10 to 11.8 m (Figure 4b), then dropped more slowly through the ice for the next two weeks until the pressure readings stabilized at 13.5 m on 1 August. The wet/dry sensor on the surface float contacted liquid water on 30 July (black star, Figure 2). We believe that the float may have been resting in a melt pond, as the upward looking images showed a highly contrasting light field indicative of heavily ponded ice (Figures 3g and 4h). The first image devoid of ice was collected on 1 September (Figure 3i); before that, small ice floes were still observed in the images (Figures 3g and 3h). The buoy drifted eastward back across the northern edge of Hanna Shoal

during the remainder of August, reversed direction in September, and drifted consistently westward through November (Figure 2).

3.2. Bio-Optical Observations

Daily integrated irradiances measured by the uppermost sensor of the WARM buoy were less than 1 mol m^{-2} d^{-1} from deployment throughout May (1 m depth; Figure 4c). Daily irradiance increased to 2–3 mol m^{-2} d^{-1} during the first week of June (Figure4c), ultimately reaching 7.8 mol m^{-2} d^{-1} on 21 June. This ~700% rise in under ice irradiance resulted largely from increased light transmission through sea ice due to snowmelt and/or surface ponding as changes in solar angle and day length only account for approximately a 20% increase in PAR for this latitude between May and July (Bernhard et al., 2007). Due to water column turbidity, the melt ponds were not visible in the daily images in June and July (Figures 3c–3e). However, the increased light availability appeared to stimulate phytoplankton growth, as [Chl *a*] determined from K_{dMID}(-PAR) also began to increase from < 0.5 to 4 mg m^{-3} in early June (Figure 4d) in association with a progressive greening of the water column recorded by the upward looking camera (Figures 3c–3f). A melt pond appears to have influenced the beneath-ice light measurements between 20 and 28 June as the irradiances at 5 m (first in-water depth) were higher than that at 1 m, and K_{dMID}(PAR) dropped suddenly (Figures 4c and 4e). Although [Chl *a*] was not available at 5 m from either the ECO triplet or the K_d(PAR) relationship during this ponding event, images taken at this time indicate increasing [Chl *a*] between 1 June and 1 July (Figures 3c–3e). In July, K_{dMID}(PAR) reached its highest value of 0.5 m^{-1} consistent with a phytoplankton bloom that reached 8.5 mg Chl m^{-3} (Figures 4d and 4e). This bloom severely attenuated light levels below 5 m compared to June, August, and September (Figure 4c).

K_{dDEEP}(PAR) increased simultaneously with K_{dMID}(PAR), indicating that growth of the phytoplankton population extended to depths beyond 10 m (Figures 4e and 4d). Light availability in August was initially ~10 mol m^{-2} d^{-1} decreasing to 2 to 4 mol m^{-2} d^{-1} at the end of the month (Figure 4c). Ice persisted in the region throughout the first half of August as indicated by the strongly contrasting light and shaded areas in the 18 August photograph (Figures 3g and 3h). [Chl *a*] levels dropped precipitously from the high values seen on 28 July to less than 2 mg m^{-3} on 29 July (Figure 4d), lowering the diffuse attenuation coefficients K_{dUPPER} (PAR) and K_{dMID}(PAR), and increasing irradiances deeper in the water column. Throughout August, K_{dDEEP} (PAR) was significantly higher (0.17 ± 0.009 m^{-1}) than K_{dMID}(PAR) (0.13 ± 0.008 m^{-1}, *t*-value = 2.9, df = 56 $p = <0.05$, Figure 3d), indicating a subsurface absorption maximum that remained in place through the fall as irradiances decreased (*t*-value = 6.8, df = 57, $p = <0.05$). In November, K_{dMID}(PAR) increased coincidently with a late fall bloom in [Chl *a*] (Figures 4d and 4e).

3.3. Modeling Under-Ice Growth of Phytoplankton

The model employed here revealed that the low light conditions through May were sufficient to support positive net carbon uptake (Figure 5b) at rates < 0.01 mmol C m^{-3} h^{-1}, leading to small growth rates defined as carbon added to the structural pool (Figure 5c), and only minimal incremental increases in Chl *a* (Figure 5d). The near quadrupling of daily light intensity beginning in June (Figures 3b and 5a) drove a period of sustained positive growth of phytoplankton biomass (Figures 5b–5d). Although irradiances remained sufficient for photosynthesis after 20 June (Figure 5b), nutrient limitation in the model (Figures 5e andf5) prevented additional growth in the uppermost 5–12 m and caused the chlorophyll maximum to deepen as growth continued on the nutricline (Figures 5c and 5d).

Model predictions of the [Chl *a*] time series generated here closely matched the buoy observations through May and predicted the initial increase in [Chl *a*] during the first 10 days of June (Figure 6). Modeled [Chl *a*] increased rapidly through June up to a maximum of 15 mg m^{-3}, almost double the observed values (Figure 6). A simulated delay in melt pond formation by 7 days (4–11 June) postponed the onset of phytoplankton growth by the same duration but did not impact the maximum biomass reached, and growth for the remainder of the season was unaffected by this short-term reduction in light intensity (Figure 6). Increasing grazing rates to 97% of net primary production reduced the peak [Chl *a*] of the bloom by about half, prolonged the bloom period, and resulted in a slower decline in phytoplankton biomass as the season progressed. If grazing was held at 44% from the start of the simulation then growth of the phytoplankton community was slower than we observed, not reaching 2 mg m^{-3} until 24 June compared to 12 June in our observations, and peak [Chl a] was not reached until 6 July (not shown). Reducing the remineralization

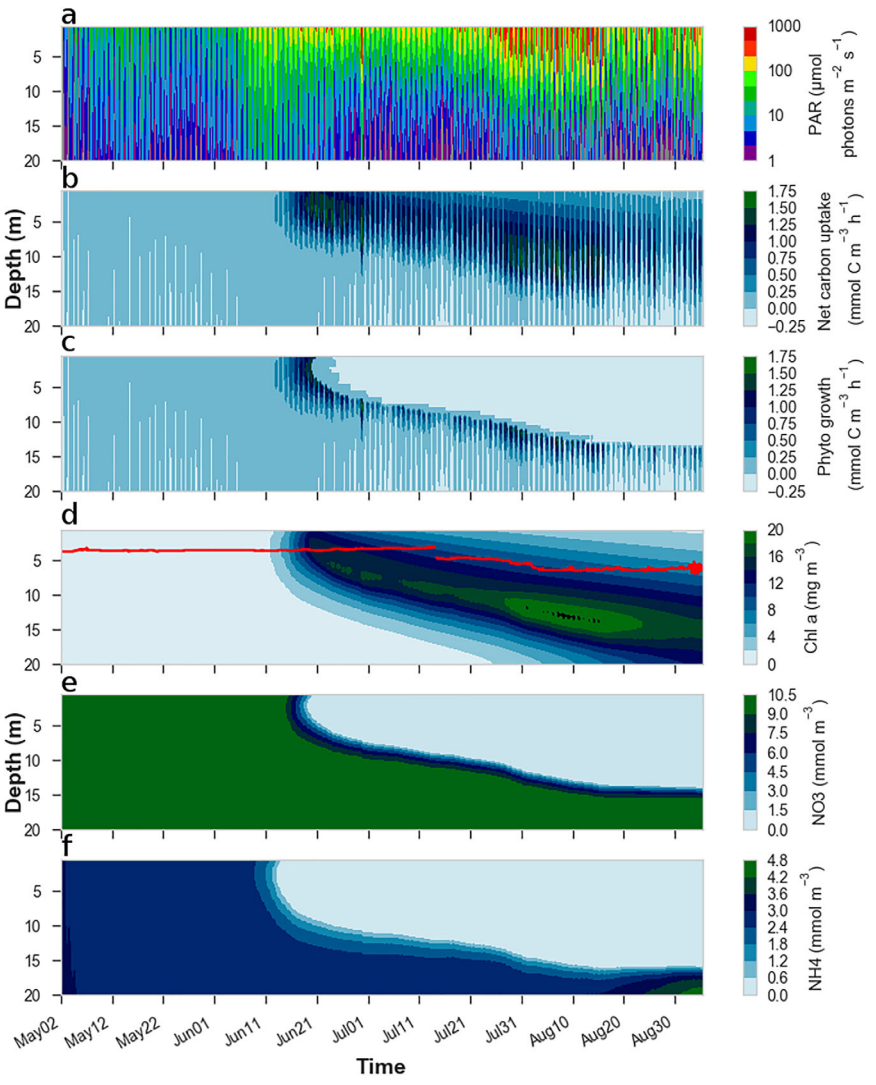

Figure 5. Predictions from the phytoplankton growth model using observed light intensities and an initial [Chl *a*] of 0.01 mg m^{-3}, the model depths are relative to the underside of the ice, and start at 0 m, the ice/water interface. (a) Modeled instantaneous irradiances (PAR), although the model was fully spectral. (b) Net photosynthetic carbon uptake. (c) Modeled phytoplankton growth represented as structural carbon added to standing stock, or lost due to respiration. (d) Modeled [Chl *a*], with an overlay of ECO triplet sensor depth over time. (e) Modeled nitrate concentration. (f) Modeled ammonium concentration. All depths displayed are relative to the underside of the ice, assuming a 2 m offset from the ocean surface. Open water conditions at the buoy were reached between 15 August and 1 September.

fraction derived from zooplankton grazing lowered peak [Chl *a*], and in the high grazing scenario resulted in a faster decline after the bloom peaked.

In the model, phytoplankton growth was driven by the light field observed by the buoy tethered to the overlying ice. However, the ice pack and the underlying water mass move independently, allowing the water column to be intermittently exposed to greater illumination than that measured by the buoy. A Landsat 8 image collected on 21 July showed that the buoy was located within loose pack ice (ice fraction >0.8, Figure 4a), with floes up to 5 km in length separated by areas of open water (Figure 7).

However, the impact of intermittent open water periods due to fluctuating ice cover on the submarine light field is nonlinearly dependent on the time of day (Figure 8a). A 24 h of open water exposure increased daily irradiance by six times over our observed under-ice environment, due to greater light transmission across the air-sea interface in the absence of ice (Figure 8a). When open water exposure exceeded 20 h, the

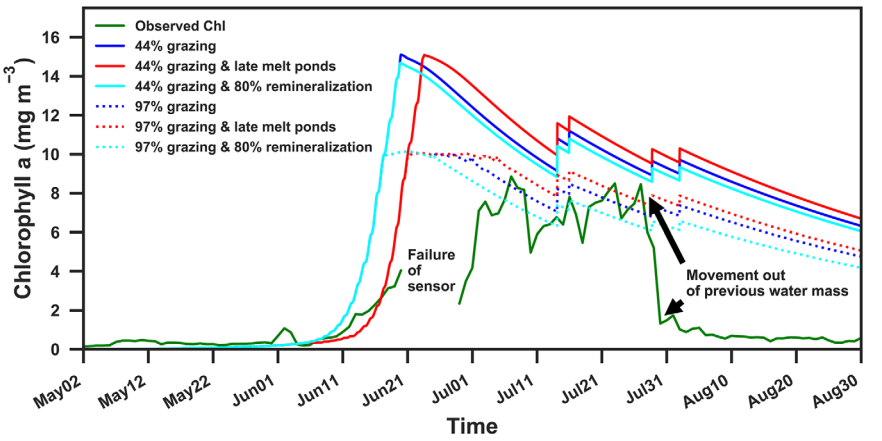

Figure 6. [Chl a] observed by the ECO triplet (green line) and modeled [Chl a] at the same depth (taking into account increases in the depth of the ECO triplet as the tether slipped through the ice), for scenarios including zooplankton grazing rates of 44% and 97% of net phytoplankton growth, observed and delayed melt pond formation, and 80% and 90% (default) remineralization rate for grazed biomass. The gap in observed [Chl a] between 15 and 30 June was caused by the transient failure of the ECO triplet system coincident with the presence of a melt pond that prevented reliable estimation of K_d(PAR) during that period. Images taken between 15 and 30 June indicate a dense bloom (Figures 3d–3f).

influence of time of day on total daily irradiance was negligible. However, 24 h of open water only increased daily integrated gross photosynthesis (P^z_{gross}) by 1.7 times when compared to the under ice regime (Figure 8b). When spending 24 h under the ice, the phytoplankton experienced photosynthesis-saturating irradiances for 56% of the day (Figure 8c). Light was only limiting under the ice between the hours of 20:00–04:00, when the sun was at its lowest elevation. Due to the 24 h of sunlight during the Arctic summer, photosynthesis was able to reach P_{max} the entire day in open water (Figure 8c). The scenario with lowest the fraction of the day spent at P_{max}, occurs when phytoplankton were under the ice during some or all of the photosynthesis limiting hours of 20:00–04:00 (Figure 8a). This caused a depression in P^z_{gross} even though daily total incident PAR is still high (Figure 8).

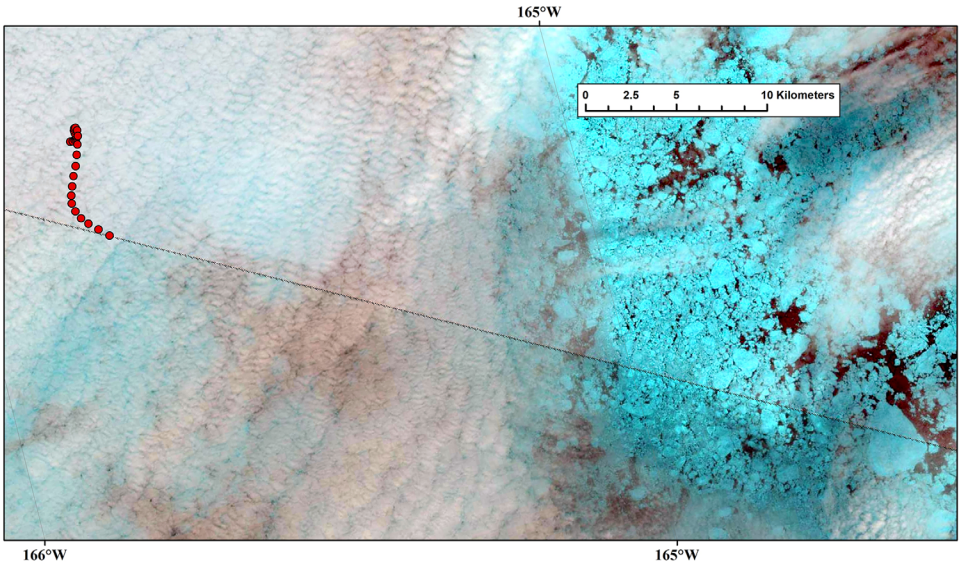

Figure 7. Landsat 8 image collected on 21 July showing ice conditions in the vicinity of the buoy. Red symbols show the location of the buoy throughout the day. Image downloaded from https://earthexplorer.usgs.gov/. Although much of the sea surface was obscured by clouds in this image, alternating patches of ice (light) and open water (dark) are apparent beneath the cloud cover in the vicinity of the buoy.

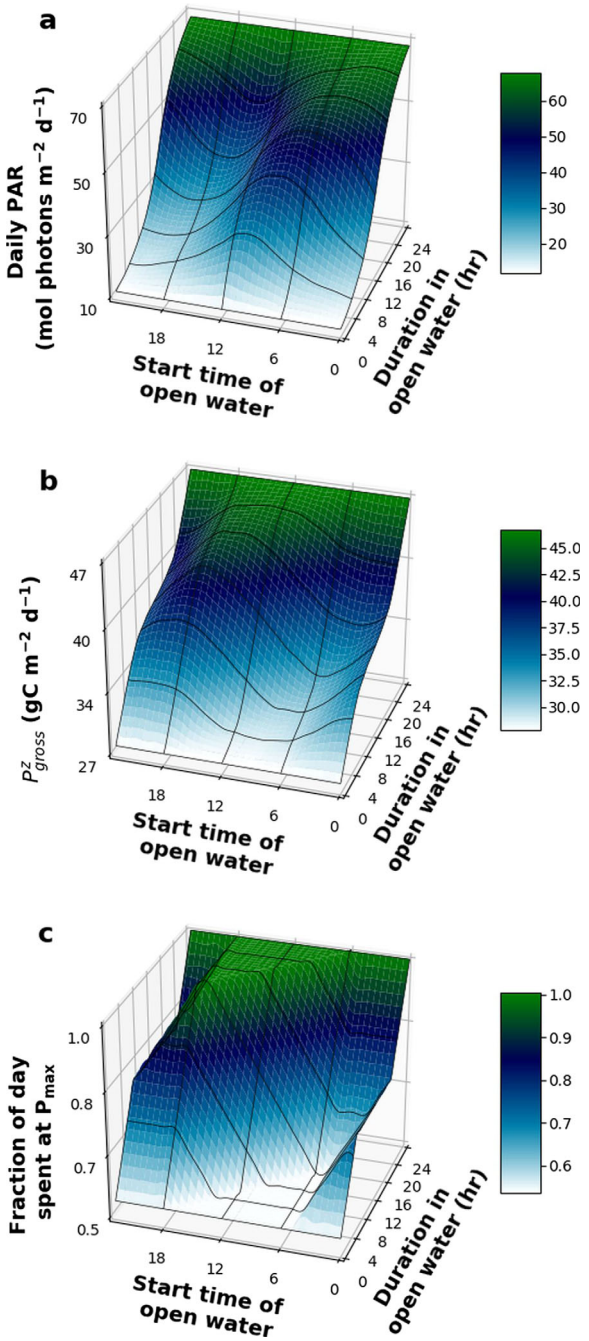

Figure 8. Modeled impacts of open water exposure on (a) Daily PAR entering the water column, (b) Depth-integrated (20 m) daily gross photosynthesis, (c) Fraction of the day spent at P_{max}.in the upper 0.5 m. These calculations assume that a start time of 12 is solar maximum and 0 is solar minimum.

4. Discussion

The high latitude of the Arctic Ocean generates seasonal extremes in light availability that become the primary factor in regulating carbon cycle dynamics. The extremely low light regime under the ice during winter and spring maintains an extended period of homogenously low water column [Chl *a*] and K_d. (Hill & Zimmerman, 2016; Pavlov et al., 2017; Pegau, 2002). Owing to the seasonal pattern of cloud cover, incident PAR is temporally asymmetrical in the Arctic, with the summer peak in irradiance delivered to the sea surface occurring approximately three weeks before the summer solstice (Bernhard et al., 2007). Consequently, advances in the onset of open water and surface melting of the ice pack that increase light transmission to the water column will also promote the development and timing of light-driven processes in the upper ocean, leading to higher productivity under the ice and in the MIZ, and reducing open water primary production (Palmer et al., 2014). Increases in light transmission to the upper ocean observed at the buoy, and attributable to snowmelt and pond formation coincided with a rapid rise in [Chl *a*] under the ice. Our bio-optical model indicated that light limitation of phytoplankton photosynthesis was lifted with the 10-fold increase in under-ice light availability, allowing for rapid phytoplankton growth. Open water between ice floes can provide sufficient integrated light exposure to allow for under-ice blooms, and this could happen earlier in the spring before melt pond formation, thus generating nutrient drawdown even though light transmission through the ice itself is low (Assmy et al., 2017). Ponded ice provides an analogous mechanism for phytoplankton to be exposed to sufficient light for positive net carbon uptake. We believe that in the case of our observations, phytoplankton growth was initially stimulated by increased light transmission through the ice rather than prolonged exposure to open water as the surrounding ice fraction was high (0.95–1.0) throughout June to mid-July 2014. The highest under-ice daily light intensities observed here (8 mol photons m_{-2} d^{-1}) were similar to those observed near the north pole ($\sim$ 7 mol photon m^{-2} d^{-1},Wang et al., 2014), showing that the potential for phytoplankton photosynthesis under the ice exists across the Arctic. P^B_E values used in the model are representative of Artic diatoms (Arrigo et al., 2014; Platt et al., 1982), and carbon uptake rates generated in the model were similar to those observed in an under ice bloom in the Chukchi Sea ($\sim$3 mmol C m^{-3} h^{-1}; Arrigo et al., 2014). Higher P^B_E such as that observed in under ice *P. pouchetii* blooms observed north of Svalbard (13 mg C mg Chl^{-1} a h^{-1}; Assmy et al., 2017), would result in higher rates of modeled growth. However, nutrients would ultimately limit growth and similar nutrient limited patterns as seen in Figure 5 would develop. As the ice pack breaks up, the upper water column can experience large temporal fluctuations in light intensity as it alternates between ice-covered and ice-free conditions. The buoy which was still connected to the ice floe through the end of August would have most likely underestimated the true light environment of the phytoplankton that are drifting in and out of ice cover. However, as shown by our model calculations, the relationship between photosynthesis and irradiance is inherently nonlinear such that increasing daily light exposure does not produce a corresponding change in P^z_{gross}. As a result of the sun remaining above the horizon in the Arctic between the beginning of May and the end of July, light intensity experienced by phytoplantkon in open water in July supported photosynthesis at P_{max} for 24 h a day. When beneath ice cover, P_{max} in our example was maintained between 06:00 and 18:00 h, thus, there was little penalty for being under the ice

during the brightest part of the day. Ice cover, however did decrease light to the extent that photosynthesis was light limited between 18:00 and 06:00 h. Consequently, being under the ice during the diurnal solar-minimum had a larger effect on daily productivity than an equivalent period under the ice during diurnal solar-maximum hours when light availability remained high enough to saturate photosynthesis.

Although the timing of modeled growth in [Chl *a*] was consistent with WARM buoy observations, the model produced more phytoplankton biomass (as [Chl *a*]) when parameterized with a 44% grazing rate than was observed by the WARM buoy. When grazing was increased to 97% of net phytoplankton growth, the model produced a more realistic [Chl *a*] peak, relative to buoy observations, amd the peak persisted as grazers remineralized some nutrients in the upper water column. Although grazing rates of 97% have been reported under ice in the Barents Sea (Verity et al., 2002) lower grazing rates between 44 and 71% of daily growth are more typically expected for the Chukchi Sea (Campbell et al., 2009; Yang et al., 2015). In fact, the region of our under-ice bloom is within an area identified as a benthic hot spot sustained by high rates of carbon transport to the benthos and low rates of pelagic grazing (Grebmeier et al., 2015a). The onset of under-ice phytoplankton blooms, combined with higher grazing rates required by the model to control phytoplankton biomass may be harbingers of change in that relationship. If under-ice blooms are consumed within the water column instead of sinking to the benthos, uncoupling of pelagic-benthic processes could be the result. Our buoy observations provided no evidence of a temporal increase in K_{dDEEP}(PAR) resulting from large quantities of sinking biomass. The shift from a sea-ice algae-benthos ecosystem to a phytoplankton-zooplankton dominated system may also be a consequence of longer open water periods which leads to prolonged phytoplankton growth, allowing zooplankton grazing and the pelagic microbial loop to limit carbon export to the benthos (Grebmeier et al., 2006; Piepenburg, 2005). Changes in the dominant phytoplankton species responsible for the majority of annual production are also possible. Under ice blooms of *Phaeocystis pouchetti* have been observed north of Svalbard taking advantage of the high open water fraction, resulting in surface nutrient drawdown and preventing later blooms of diatoms (Assmy et al., 2017). It is unclear, however, how this shift from diatoms to prymnesiophytes will affect the biological carbon pump that is critical to benthic production on the Chukchi Shelf (Nejstgaard et al., 2007).

Initializing the model runs with lower nutrient concentrations would have reduced the magnitude of the modeled [Chl *a*] peak. However, initial nutrient concentrations were consistent with known wintertime concentrations of NO_3^- and PO_4^{-3} for this region (Codispoti et al., 2005; Lowry et al., 2015). The development of a subsurface peak in [Chl *a*] observed by the buoy was reproduced by the model as a result of nutrient limitation in the upper 10 m of the water column. This subsurface feature is commonly found in this area in July and August following the decay of the original spring bloom (Ardyna et al., 2013; Hill et al., 2013; Martini et al., 2016; McLaughlin & Carmack, 2010). The bloom observed during July was approximately 50–200 km into the ice pack from the ice edge, in the same area and period as the sizable under-ice bloom observed by the 2011 ICESCAPE mission (Arrigo et al., 2012; Churnside & Marchbanks, 2015). Water masses in this area are derived from the nutrient-rich winter water flowing across the area west of Hanna Shoal after draining Herald Canyon and the Central Channel (Lowry et al., 2015). Given the plentiful late winter nutrient pool in the northeastern Chukchi Sea (Arrigo et al., 2017), this region is primed for the development of algae blooms, requiring only sufficient light availability under the ice. The same increase in light to the upper water column in nutrient-limited regions such as the East Siberian Sea and Canada Basin will not result in such dense phytoplankton blooms (Hill et al., 2017).

In a future Arctic in which under-ice blooms are common, nutrient limitation in the surface mixed layer after ice retreat will suppress primary production as seen in our model, producing vertical distributions that are more representative of post-bloom summer conditions, including low surface productivity and a subsurface biomass peak on the nitracline (Ardyna et al., 2013; Hill et al., 2017; Martin et al., 2010). Open water production could be increased through the summer via mechanisms that bring nutrients up into the surface mixed layer. These include vertical mixing due to expanded open water conditions, which increases the fetch and could periodically mix nutrients up to the surface and strong easterly winds that induce upwelling of nutrient-rich water from the deep Canada Basin (Spall et al., 2014). In regions that have just recently experienced ice-free summers such as the oligotrophic basins of the Arctic, nitrate concentrations within the euphotic zone are nearly undetectable even in winter (Codispoti et al., 2013; Varela et al., 2013). Thus, the increased light penetration and longer growing season resulting from sea ice retreat will not result in increases in annual productivity unless changes in circulation, shoaling of the Atlantic water mass layer, or

the potential impact of atmospheric forcing in the form of storms and waves could erode the vertical stratification providing a source of nutrients to the upper water column (Rainville & Woodgate, 2009; Rainville et al., 2011).

Our observations using the WARM buoy system provide evidence that light availability was sufficient to support high phytoplankton growth rates beneath seasonal sea ice cover in the Arctic Ocean. The mechanistic confirmation provided by our bio-optical model provides further evidence that dense phytoplankton populations recently observed under the ice (Arrigo et al., 2012; Assmy et al., 2017; Churnside & Marchbanks, 2015) are likely to have grown in place and were not laterally advected from ice-free areas. As seasonal ice cover becomes more dominant in the Arctic, its thinner snow cover which is more quickly melted will be the primary agent in determining the magnitude of the under-ice light field, followed by ice thickness and earlier surface melt pond formation. The higher light transmission through younger ice makes it increasingly likely that phytoplankton growth beneath the ice can be initiated before the arrival of open water. In addition to changing predator-prey relations and carbon export to shelf sediments by altering the timing of phytoplankton growth, increased solar energy will likely increase the rates of other processes including solar driven warming and ice melt, water column stratification with subsequent impacts on nutrient replenishment and photochemical oxidation of DOM with influences on the microbial loop. Autonomous ice-based systems can provide key quantitative information on critical oceanographic processes during the spring when extensive ice cover limits opportunities for ship-based observations and satellite remote sensing to investigate the dynamics of ocean primary production in the context of a changing climate.

Acknowledgments
This study was funded by NSF Office of Polar Programs through grants ARC 1603548 & 1203440, and PLR 1203784 &1602521. Our thanks to the staff at UIC Science LLC in Utqiaġvik and Polar Field Services for logistics support. All data from the buoy are publicly available at the NSF Arctic Data Center (https://arcticdata.io/catalog/#view/doi:10.18739/A2J954).

References

Ardyna, M., Babin, M., Gosselin, M., Devred, E., Belanger, S., Matsuoka, A., et al. (2013). Parameterization of vertical chlorophyll a in the Arctic Ocean: Impact of the subsurface chlorophyll maximum on regional, seasonal, and annual primary production estimates. *Biogeosciences*, *10*(6), 4383–4404. https://doi.org/10.5194/bg-10-4383-2013

Arrigo, K. R., Mills, M. M., Van Dijken, G., Lowry, K. E., Pickart, R. S., & Schlitzer, R. (2017). Late Spring Nitrate Distributions Beneath the Ice-Covered Northeastern Chukchi Shelf. *Journal of Geophysical Research: Biogeosciences*, *122*, 2409–2417. https://doi.org/10.1002/2017JG003881

Arrigo, K. R., Perovich, D. K., Pickart, R. S., Brown, Z. W., Van Dijken, G. L., Lowry, K. E., et al. (2012). Massive phytoplankton blooms under Arctic sea ice. *Science*, *336*, 1408. https://doi.org/10.1126/science.1215065

Arrigo, K. R., Perovich, D. K., Pickart, R. S., Brown, Z. W., van Dijken, G. L., Lowry, K. E., et al. (2014). Phytoplankton blooms beneath the sea ice in the Chukchi sea. *Deep Sea Research Part II: Topical Studies in Oceanography*, *105*, 1–16. https://doi.org/10.1016/j.dsr2.2014.03.018

Assmy, P., Fernandez-Mendez, M., Duarte, P., Meyer, A., Randelhoff, A., Mundy, C. J., et al. (2017). Leads in Arctic pack ice enable early phytoplankton blooms below snow-covered sea ice. *Scientific Reports*, *7*, 40850. https://doi:10.1038/srep40850

Beitsch, A., Kaleschke, L., & Kern, S. (2014). Investigating high-resolution AMSR2 sea ice concentrations during the February 2013 fracture event in the Beaufort sea. *Remote Sensing*, *6*(5), 3841–3856. https://doi.org/10.3390/rs6053841

Bernhard, G., Booth, C. R., Ehramjian, J. C., Stone, R., & Dutton, E. G. (2007). Ultraviolet and visible radiation at Barrow, Alaska: Climatology and influencing factors on the basis of version 2 National Science Foundation network data. *Journal of Geophysical Research*, *112*, D09101. https://doi.org/10.1029/2006JD007865

Bricaud, A., Babin, M., Morel, A., & Claustre, H. (1995). Variability in the chlorophyll-specific absorption coefficients of natural phytoplankton: Analysis and parameterizaton absorption. *Journal of Geophysical Research*, *100*(C7), 13321–13332. https://doi.org/10.1029/95JC00463

Campbell, R. G., Sherr, E. B., Ashjian, C. J., Plourde, S., Sherr, B. F., Hill, V., et al. (2009). Mesozooplankton prey preference and grazing impact in the western Arctic Ocean. *Deep-Sea Research Part II: Topical Studies in Oceanography*, *56*(17), 1274–1289. https://doi.org/10.1016/j.dsr2.2008.10.027

Churnside, J. H., & Marchbanks, R. D. (2015). Subsurface plankton layers in the Arctic Ocean. *Geophysical Research Letters*, *42*, 4896–4902. https://doi.org/10.1002/2015GL064503

Codispoti, L. A., Flagg, C., & Kelly, V. (2005). Hydrographic conditions during the 2002 SBI process experiments. *Deep Sea Research Part II: Topical Studies in Oceanography*, *52*, 3199–3226

Codispoti, L. A., Kelly, V., Thessen, A., Matrai, P., Suttles, S., Hill, V., et al. (2013). Synthesis of primary production in the Arctic Ocean: III. Nitrate and phosphate based estimates of net community production. *Progress in Oceanography*, *110*, 126–150. https://doi.org/10.1016/j.pocean.2012.11.006

Comiso, J. C. (2012). Large decadal decline of the arctic multiyear ice cover. *Journal of Climate*, *25*(4), 1176–1193. https://doi.org/10.1175/Jcli-D-11-00113.1

Ehn, J. K., & Mundy, C. J. (2013). Assessment of light absorption within highly scattering bottom sea ice from under-ice light measurements: Implications for Arctic ice algae primary production. *Limnology and Oceanography*, *58*(3), 893–902. https://doi.org/10.4319/lo.2013.58.3.0893

Ehn, J. K., Mundy, C. J., Barber, D. G., Hop, H., Rossnagel, A., & Stewart, J. (2011). Impact of horizontal spreading on light propagation in melt pond covered seasonal sea ice in the Canadian Arctic. *Journal of Geophysical Research*, *116*, C00G02. https://doi.org/10.1029/2010JC006908

Eicken, H. (2016). *Automated ice mass balance site (SIZONET)*. NSF Arctic Data Center. https://doi.org/10.18739/A2D08X

Emerson, R., & Lewis, C. M. (1943). The dependence of the quantum yield of chlorella photosynthesis on wave length of light. *American Journal of Botany*, *30*(3), 165–178. https://doi.org/0.2307/2437236

Forest, A., Tremblay, J. E., Gratton, Y., Martin, J., Gagnon, J., Darnis, G., et al. (2011). Biogenic carbon flows through the planktonic food web of the Amundsen Gulf (Arctic Ocean): A synthesis of field measurements and inverse modeling analyses. *Progress in Oceanography*, *91*(4), 410–436. https://doi.org/10.1016/j.pocean.2011.05.002

Frey, K. E., Perovich, D. K., & Light, B. (2011). The spatial distribution of solar radiation under a melting Arctic sea ice cover. *Geophysical Research Letters*, *38*. https://doi.org/10.1029/2011gl049421.

Frey, K. E., Moore, G. W. K., Cooper, L. W., & Grebmeier, J. M. (2015). Divergent patterns of recent sea ice cover across the Bering, Chukchi, and Beaufort seas of the Pacific Arctic Region. *Progress in Oceanography*, *136*, 32–49. https://doi.org/10.1016/j.pocean.2015.05.009

Grebmeier, J. M., Bluhm, B. A., Cooper, L. W., Denisenko, S. G., Iken, K., Kedra, M., et al. (2015a). Time-series benthic community composition and biomass and associated environmental characteristics in the Chukchi Sea During the RUSALCA 2004–2012 program. *Oceanography*, *28*(3), 116–133. https://doi.org/10.5670/oceanog.2015.61

Grebmeier, J. M., Cooper, L. W., Feer, H. M., & Sirenko, B. I. (2006). Ecosystem dynamics of the Pacific-influenced Northern Bering and Chukchi Seas in the Amerasian Arctic. *Progress in Oceanography*, *71*(2–4), 331–361.

Grebmeier, J. M., Cooper, L. W., Ashjian, C. J., Bluhm, B. A., Campbell, R. B., Dunton, K., et al. (2015b). *Pacific Marine Arctic Regional Synthesis (PacMARS)* (final report, 259 pp.). Anchorage, AK: North Pacific Research Board.

Grenfell, T. C., & Perovich, D. K. (2004). Seasonal and spatial evolution of albedo in a snow-ice-land-ocean environment. *Journal of Geophysical Research*, *109*, C01001. https://doi.org/10.1029/2003JC001866

Hill, V. (2004). *The Western Arctic Shelf-Basin Interactions (SBI) experiment contains measurements made in the Chukchi and Beaufort seas off the coast of northern Alaska*. NASA SeaBASS. https://doi.org/10.5067/SeaBASS/SBI/DATA001. Retrieved from https://www.eol.ucar.edu/projects/sbi/index.html

Hill, V. J., Matrai, P. A., Olson, E., Suttles, S., Steele, M., Codispoti, L. A., & Zimmerman, R. C. (2013). Synthesis of integrated primary production in the Arctic Ocean: II. In situ and remotely sensed estimates. *Progress in Oceanography*, *110*, 107–125. https://doi.org/10.1016/j.pocean.2012.11.005

Hill, V., Ardyna, M., Lee, S. H., & Varela, D. E. (2017). Decadal trends in phytoplankton production in the Pacific Arctic Region from 1950 to 2012. *Deep Sea Research Part II: Topical Studies in Oceanography*. in press, https://doi.org/10.1016/j.dsr2.2016.12.015

Hill, V., Steele, M., & Light, B. (2016). *Warming and irradiance measurements in the Arctic: Determining the link between solar energy absorption and surface warming through long term observations*. NSF Arctic Data Center. https://arcticdata.io/catalog/#view/doi:10.18739/A2J954

Hill, V. J. (2008). Impacts of chromophoric dissolved organic material on surface ocean heating in the Chukchi Sea. *Journal of Geophysical Research*, *113*, C07024. https://doi.org/10.1029/2007JC004119

Hill, V. J., & Zimmerman, R. C. (2016). Characteristics of colored dissolved organic material in first year landfast sea ice and the underlying water column in the Canadian Arctic in the early spring. *Marine Chemistry*, *180*, 1–13. https://doi.org/10.1016/j.marchem.2016.01.007

Horvat, C., Jones, D. R., Iams, S., Schroeder, D., Flocco, D., & Feltham, D. (2017). The frequency and extent of sub-ice phytoplankton blooms in the Arctic Ocean. *Science Advances*, *3*(3), e1601191. https://doi.org/10.1126/sciadv.1601191

Hudson, S. R., Granskog, M. A., Sundfjord, A., Randelhoff, A., Renner, A. H. H., & Divine, D. V. (2013). Energy budget of first-year Arctic sea ice in advanced stages of melt. *Geophysical Research Letters*, *40*, 2679–2683. https://doi.org/10.1002/grl.50517

Itkin, P., Spreen, G., Cheng, B., Doble, M., Girard-Ardhuin, F., Haapala, J., et al. (2017). Thin ice and storms: Sea ice deformation from buoy arrays deployed during N-ICE2015. *Journal of Geophysical Research: Oceans*, *122*, 4661–4674. https://doi.org/10.1002/2016JC012403

Ji, R. B., Jin, M. B., & Varpe, O. (2013). Sea ice phenology and timing of primary production pulses in the Arctic Ocean. *Global Change Biology*, *19*(3), 734–741. https://doi.org/10.1111/gcb.12074

Katlein, C., Nicolaus, M., & Petrich, C. (2014). The anisotropic scattering coefficient of sea ice. *Journal of Geophysical Research: Oceans*, *119*, 842–855. https://doi.org/10.1002/2013JC009502

Kirk, J. T. O. (1994). *Light and photosynthesis in aquatic ecosystems photosynthesis*. Cambridge. UK: Cambridge University Press,

Kwok, R., & Rothrock, D. A. (2009). Decline in Arctic sea ice thickness from submarine and ICESat records: 1958–2008. *Geophysical Research Letters*, *36*, L15501. https://doi.org/10.1029/2009GL039035

Laney, S. R., Krishfield, R. A., & Toole, J. M. (2017). The euphotic zone under Arctic Ocean sea ice: Vertical extents and seasonal trends. *Limnology and Oceanography*, *62*(5), 1910–1934. https://doi.org/10.1002/lno.10543

Laney, S. R., Krishfield, R. A., Toole, J. M., Hammar, T. R., Ashjian, C. J., & Timmermans, M. L. (2014). Assessing algal biomass and bio-optical distributions in perennially ice-covered polar ocean ecosystems. *Polar Science*, *8*(2), 73–85. https://doi.org/10.1016/j.polar.2013.12.003

Laws, E. A. (1991). Photosynthetic quotients, new production and net community production in the open ocean. *Deep Sea Research Part A: Oceanographic Research Papers*, *38*(1), 143–167. https://doi.org/10.1016/0198-0149(91)90059-O

Lee, Z., Weidemann, A., Kindle, J., Arnone, R., Carder, K. L., & Davis, C. (2007). Euphotic zone depth: Its derivation and implication to ocean-color remote sensing. *Journal of Geophysical Research*, *112*, C03009. https://doi.org/10.1029/2006JC003802

Lee, Z. P., Du, K. P., & Arnone, R. (2005). A model for the diffuse attenuation coefficient of downwelling irradiance. *Journal of Geophysical Research*, *110*, C02016. https://doi.org/10.1029/2004JC002275

Leu, E., Soreide, J. E., Hessen, D. O., Falk-Peterson, S., & Berge, J. (2011). Consequences of changing sea-ice cover for primary and secondary producers in the European Arctic shelf seas: Timing, quantity, and quality. *Progress in Oceanography*, *90*, 18–32.

Light, B., Perovich, D. K., Webster, M. A., Polashenski, C., & Dadic, R. (2015). Optical properties of melting first-year Arctic sea ice. *Journal of Geophysical Research: Oceans*, *120*, 7657–7675. https://doi.org/10.1002/2015JC011163

Lindsay, R., & Schweiger, A. (2015). Arctic sea ice thickness loss determined using subsurface, aircraft, and satellite observations. *Cryosphere*, *9*(1), 269–283. https://doi.org/10.5194/tc-9-269-2015

Lowry, K. E., Pickart, R. S., Mills, M. M., Brown, Z. W., van Dijken, G. L., Bates, N. R., et al. (2015). The influence of winter water on phytoplankton blooms in the Chukchi Sea. *Deep Sea Research Part II: Topical Studies in Oceanography*, *118*, 53–72. https://doi.org/10.1016/j.dsr2.2015.06.006

Martin, J., Tremblay, J.-E., Gagnon, J., Tremblay, G., Lapoussiere, A., Jose, C., et al. (2010). Prevalence, structure and properties of subsurface chlorophyll maxima in Canadian Arctic waters Canadian Arctic. *Marine Ecology Progress Series*, *42*, 69–84. https://doi.org/10.3354/meps08666

Martini, K. I. P., Stabeno, P. J., Ladd, C., Winsor, P., Weingartner, T., Mordy, C. W., & Eisner, L. B. (2016). Dependence of subsurface chlorophyll on seasonal water masses in the Chukchi Sea. *Journal of Geophysical Research*, *121*. https://doi.org/10.1002/2015JC011359

Matuszko, D. (2012). Influence of the extent and genera of cloud cover on solar radiation intensity. *International Journal of Climatology*, *32*(15), 2403–2414. https://doi.org/10.1002/joc.2432

McLaughlin, F. A., & Carmack, E. C. (2010). Deepening of the nutricline and chlorophyll maximum in the Canada Basin interior, 2003–2009. *Geophysical Research Letters*, *37*. https://doi.org/10.1029/2010gl045459

Merkouriadi, I., Cheng, B., Graham, R. M., Rosel, A., & Granskog, M. (2017). Critical role of snow on sea ice growth in the Atlantic sector of the Arctic Ocean. *Geophysical Research Letters*, *44*, 10,479–10,485. https://doi.org/10.1002/2017GL075494

Moran, S. B., Kelly, R. P., Hagstrom, K., Smith, J. N., Grebmeier, J. M., Cooper, L. W., et al. (2005). Seasonal changes in POC export flux in the Chukchi Sea and implications for water column-benthic coupling in Arctic shelves. *Deep Sea Research Part II: Topical Studies in Oceanography*, *52*(24–26), 3427–3451. https://doi.org/10.1016/j.dsr2.2005.09.011

Nejstgaard, J. C., Tang, K. W., Steinke, M., Dutz, J., Koski, M., Antajan, E., et al. (2007). Zooplankton grazing on Phaeocystis: A quantitative review and future challenges. *Biogeochemistry*, *83*(1–3), 147–172. https://doi.org/10.1007/s10533-007-9098-y

Nicolaus, M., Gerland, S., Hudson, S. R., Hanson, S., Haapala, J., & Perovich, D. K. (2010b). Seasonality of spectral albedo and transmittance as observed in the Arctic Transpolar Drift in 2007. *Journal of Geophysical Research*, *115*, C11011. https://doi.org/10.1029/2009JC006074

Nicolaus, M., Hudson, S. R., Gerland, S., & Munderloh, K. (2010a). A modern concept for autonomous and continuous measurements of spectral albedo and transmittance of sea ice. *Cold Regions Science and Technology*, *62*, 24. https://doi.org/10.1016/j.coldregions.2010.03.001

Nicolaus, M., Katlein, C., Maslanik, J., & Hendricks, S. (2012). Changes in Arctic sea ice result in increasing light transmittance and absorption. *Geophysical Research Letters*, *39*, L24501. https://doi.org/10.1029/2012GL053738

Nicolaus, M., Petrich, C., Hudson, S. R., & Granskog, M. A. (2013). Variability of light transmission through Arctic land-fast sea ice during spring. *Cryosphere*, *7*(3), 977–986. https://doi.org/10.5194/tc-7-977-2013

Palmer, M. A., Saenz, B. T., & Arrigo, K. R. (2014). Impacts of sea ice retreat, thinning, and melt-pond proliferation on the summer phytoplankton bloom in the Chukchi Sea, Arctic Ocean. *Deep Sea Research Part II: Topical Studies in Oceanography*, *105*, 85–104. https://doi.org/10.1016/j.dsr2.2014.03.016

Pavlov, A. K., Taskjelle, T., Kauko, H. M., Hamre, B., Hudson, S. R., Assmy, P., et al. (2017). Altered inherent optical properties and estimates of the underwater light field during an Arctic under-ice bloom of Phaeocystis pouchetii. *Journal of Geophysical Research: Oceans*, *122*, 4939–4961. https://10.1002/2016JC012471

Pegau, W. S. (2002). Inherent optical properties of the central Arctic surface waters. *Journal of Geophysical Research*, *107*(C10), 8035. https://doi.org/doi.org/10.1029/2000JC000382

Peng, G., Meier, W. N., Scott, D. J., & Savoie, M. H. (2013). A long-term and reproducible passive microwave sea ice concentration data record for climate studies and monitoring. *Earth System Science Data*, *5*(2), 311–318. https://10.5194/essd-5-311-2013

Perovich, D. K. (2007). Light reflection and transmission by a temperate snow cover. *Journal of Glaciology*, *53*(181), 201–210. https://doi.org/10.3189/172756507782202919

Perovich, D. K., & Polashenski, C. (2012). Albedo evolution of seasonal Arctic sea ice. *Geophysical Research Letters*, *39*. https://doi.org/10.1029/2012gl051432

Piepenburg, D. (2005). Recent research on Arctic benthos: Common notions need to be revised. *Polar Biology*, *28*(10), 733–755. https://doi.org/10.1007/s00300-005-0013-5

Platt, T., Harrison, W. G., Irwin, B., Horne, E. P., & Gallegos, C. L. (1982). Photosynthesis and Photoadaptation of Marine-Phytoplankton in the Arctic. *Deep Sea Research Part A: Oceanographic Research Papers*, *29*(10), 1159–1170. https://doi.org/10.1016/0198-0149(82)90087-5

Polashenski, C., Perovich, D., & Courville, Z. (2012). The mechanisms of sea ice melt pond formation and evolution. *Journal of Geophysical Research*, *117*, C01001. https://doi.org/10.1029/2011JC007231

Pope, R., & Fry, M. E. S. (1997). Absorption spectrum (380– 700 nm) of pure water. Part II: Integrating cavity measurements. *Applied Optics*, *36*, 8710–8723. https://doi.org/10.1364/AO.36.008710

Rainville, L., Lee, C. M., & Woodgate, R. A. (2011). Impact of wind-driven mixing in the Arctic Ocean. *Oceanography*, *24*(3), 136–145. https://doi.org/10.5670/oceanog.2011.65

Rainville, L., & Woodgate, R. A. (2009). Observations of internal wave generation in the seasonally ice-free Arctic. *Geophysical Research Letters*, *36*, L23604. https://doi.org/10.1029/2009GL041291

Reynolds, R. A., Stramski, D., & Mitchell, B. G. (2001). A chlorophyll-dependent semianalytical reflectance model dervived from field measurements of absorption and backscattering coefficients within the Southern Ocean. *Journal of Geophysical Research*, *106*(C4), 7125–7138. https://doi.org/10.1029/1999JC000311

Richter-Menge, J. A., & Farrell, S. L. (2013). Arctic sea ice conditions in spring 2009–2013 prior to melt. *Geophysical Research Letters*, *40*, 5888–5893. https://doi.org/10.1002/2013GL058011

Roesler, C. S., Perry, M. J., & Carder, K. L. (1989). Modeling in situ phytoplankton absorption from total absorption spectra in productive inland marine waters. *Limnology and Oceanography*, *34*(8), 1510–1523. https://doi.org/10.4319/lo.1989.34.8.1510

Soreide, J. E., Leu, E., Berge, J., Graeve, M., & Falk-Petersen, S. (2010). Timing of blooms, algal food quality and Calanus glacialis reproduction and growth in a changing Arctic. *Global Change Biology*, *16*(11), 3154–3163. https://doi.org/10.1111/j.1365-2486.2010.02175.x

Spall, M. A., Pickart, R. S., Brugler, E. T., Moore, G. W. K., Thomas, L., & Arrigo, K. R. (2014). Role of shelfbreak upwelling in the formation of a massive under-ice bloom in the Chukchi Sea. *Deep Sea Research Part II: Topical Studies in Oceanography*, *105*, 17–29. https://10.1016/j.dsr2.2014.03.017

Spreen, G., Kaleschke, L., & Heygster, G. (2008). Sea ice remote sensing using AMSR-E 89-GHz channels. *Journal of Geophysical Research*, *113*, C02S03. https://doi.org/10.1029/2005JC003384

Vaquer-Sunyer, R., Duarte, C. M., Santiago, R., Wassmann, P., & Reigstad, M. (2010). Experimental evaluation of planktonic respiration response to warming in the European Arctic Sector. *Polar Biology*, *33*(12), 1661–1671. https://doi.org/10.1007/s00300-010-0788-x

Varela, D. E., Crawford, D. W., Wrohan, I. A., Wyatt, S. N., & Carmack, E. C. (2013). Pelagic primary productivity and upper ocean nutrient dynamics across Subarctic and Arctic Seas. *Journal of Geophysical Research*, *118*, 7132–7152. https://10.1002/2013JC009211

Verity, P. G., Wassmann, P., Frischer, M. E., Howard-Jones, M. H., & Allen, A. E. (2002). Grazing of phytoplankton by microzooplankton in the Barents Sea during early summer. *Journal of Marine Systems*, *38*(1–2), 109–123. https://doi.org/10.1016/S0924-7963(02)00172-0

Wang, C. X., Granskog, M. A., Gerland, S., Hudson, S. R., Perovich, D. K., Nicolaus, M., et al. (2014). Autonomous observations of solar energy partitioning in first-year sea ice in the Arctic Basin. *Journal of Geophysical Research: Oceans*, *119*, 2066–2080. https://doi.org/10.1002/2013JC009459

Wang, C. X., Granskog, M. A., Hudson, S. R., Gerland, S., Pavlov, A. K., Perovich, D. K., et al. (2016). Atmospheric conditions in the central Arctic Ocean through the melt seasons of 2012 and 2013: Impact on surface conditions and solar energy deposition into the ice-ocean system. *Journal of Geophysical Research: Atmospheres*, *121*, 1043–1058. https://doi.org/10.1002/2015JD023712

Webster, M. A., Rigor, I. G., Nghiem, S. V., Kurtz, N. T., Farrell, S. L., Perovich, D. K., & Sturm, M. (2014). Interdecadal changes in snow depth on Arctic sea ice. *Journal of Geophysical Research-Oceans*, *119*(8), 5395–5406. https://doi.org/10.1002/2014JC009985

Wang, J., Cota, G. F., & Ruble, D. A. (2005). Absorption and backscattering in the Beaufort and Chukchi Seas Chukchi Sea. *Journal of Geophysical Research*, *110*, C04014. https://doi.org/10.1029/2002JC001653

Yang, E. J., Ha, H. K., & Kang, S. H. (2015). Microzooplankton community structure and grazing impact on major phytoplankton in the Chukchi sea and the western Canada basin, Arctic ocean. *Deep Sea Research Part II: Topical Studies in Oceanography*, *120*, 91–102. https://doi.org/10.1016/j.dsr2.2014.05.020

Zimmerman, R. C., Hill, V. J., & Gallegos, C. L. (2015). Predicting effects of ocean warming, acidification, and water quality on Chesapeake region eelgrass. *Limnology and Oceanography*, *60*(5), 1781–1804. https://doi.org/10.1002/lno.10139